ASME Journal of Applied Mechanics
Online journal at:
https://asmedigitalcollection.asme.org/appliedmechanics

Ruojun Zhang
Key Laboratory of Dynamics and Control of Flight Vehicle of Ministry of Education, School of Aerospace Engineering, Beijing Institute of Technology, Beijing 100081, China;
Chinese Aeronautical Establishment, Beijing 100029, China
e-mail: ruojunzhang@126.com

Lei Zhang
Key Laboratory of Dynamics and Control of Flight Vehicle of Ministry of Education, School of Aerospace Engineering, Beijing Institute of Technology, Beijing 100081, China
e-mail: 3120246324@bit.edu.cn

Gengkai Hu
Key Laboratory of Dynamics and Control of Flight Vehicle of Ministry of Education, School of Aerospace Engineering, Beijing Institute of Technology, Beijing 100081, China
e-mail: hugeng@bit.edu.cn

Xiaoming Zhou[1]
Key Laboratory of Dynamics and Control of Flight Vehicle of Ministry of Education, School of Aerospace Engineering, Beijing Institute of Technology, Beijing 100081, China
e-mail: zhxming@bit.edu.cn

Sound Mitigation by Metamaterials With Low-Transmission Flat Band

Space-coiling acoustic metamaterials dominated by the Fano resonance are being widely exploited for simultaneous control of sound isolation and air ventilation, and they usually achieve complete sound mitigation at multiple isolated frequencies. Here, we theoretically discover and experimentally demonstrate the low-transmission flat-band phenomenon in channeling-type acoustic metamaterials. The metamaterial is constructed with coupled coiling and straight channels, both working in acoustic resonant states. An analytic coupled-mode model is established to capture the coupling interaction between resonant states supported by two channels. A critical coupling condition is derived from the model, which can lead to sextremely low sound transmission in a finite band rather than at isolated frequencies, as validated by both numerical simulations and experiments. We then demonstrate the generality of the flat-band behavior of low transmission by a systematic survey of the coupling of different order resonant modes. Finally, the flat-band effect is also found to exist in the extended model with the side-loaded coiling channel as verified experimentally. [DOI: 10.1115/1.4067207]

Keywords: acoustic metamaterials, sound isolation, air ventilation, coupled-mode theory, resonant coupling, dynamics, structures, wave propagation

1 Introduction

Acoustic metamaterials are artificial materials engineered to have acoustic properties superior to conventional materials. By the careful design of subwavelength microstructures, acoustic metamaterials can be created to possess exotic wave control ability such as wavefront modulation [1–3], subdiffraction imaging [4,5], and acoustic cloaking [6–8]. In noise control engineering, acoustic attenuation in the broadband and low-frequency regime is in great demand, and the air flow ventilation in addition to sound isolation is also required in some circumstances [9–11]. In the past decade, acoustic metamaterials were developed to improve the sound isolation and absorption performance, showing great potential for noise control applications. A widely explored mechanism for sound reduction is based on the local resonance effect of acoustic metamaterials [12–21]. The local resonance can cause strong wave interference at the subwavelength scale; thus, the frequency at which the resonance occurs can be greatly lowered, leading to the low-frequency sound-reduction control. However, the working bandwidth is narrow due to the strong dispersion associated to the local resonance. To broaden the working bandwidth, the multiple-resonance method is usually adopted in acoustic metamaterial design by combining structural elements with different working frequencies [22–29]. Enough volume space is often required for acoustic metamaterials to assemble multiple elements [30,31].

Recently, acoustic metamaterials made of space-coiling channels have undergone a rapid development toward the simultaneous control of sound isolation and air ventilation. As a basic model, a coiling channel that works in the resonant state is coupled to a straight ventilation pipe, which acts as a continuous state. The interference between them can form the Fano resonance, which enables high-performance sound isolation in a finite bandwidth while preserving the air ventilation. Based on the Fano interference behavior, ventilated acoustic insulators can be designed by acoustic metamaterials with channels coiled along the radial [32] or circumferential [33,34] directions. The Fano-resonance metamaterials also possess the ability for omnidirectional sound attenuation with the effectiveness to block sounds from various incident directions [35] or work in reverberant environment with diffuse fields [36]. Assisted by the

[1]Corresponding author.
Manuscript received October 16, 2024; final manuscript received November 13, 2024; published online December 5, 2024. Tech. Editor: Pradeep Sharma.

machining learning and optimization design, the sound-isolation bandwidth of space-coiling metamaterials can be broadened by coupling two Fano resonances, realizing an ultra-broadband low-frequency sound attenuation [37,38]. The resonant coupling of acoustic modes together with the Fano resonance can provide another route to broaden the sound-reduction bandwidth [39,40].

The Fano-based models can only achieve complete sound mitigation at multiple isolated frequencies, and the broadband behavior of sound reduction is acquired by minimizing acoustic transmission between those frequencies. In this work, we report a novel mechanism to realize the near-zero sound transmission in a finite band rather than at specific frequencies. Acoustic metamaterial supporting this behavior is composed of the coupled coiling and straight channels that both operate in resonant states. The condition for producing the flat-band effect is derived by using the coupled-mode model. The generality of the low-transmission flat-band phenomenon is revealed in metamaterials with the coupling of different order resonant modes, and metamaterials with the different arrangements of the coiling channel that can be placed either internally or externally with respect to the wave-guiding system.

2 Theoretical Modeling

2.1 Geometric Model. Consider a rectangular waveguide of the height l_x and width l_y internally coupled to a coiling channel of the width a_2 and length L_2 as well as a straight channel of the width a_1 and length L_1, which have the same height h, as schematically shown in Fig. 1(*a*). A plane acoustic wave of angular frequency ω is normally incident on the channeling structure. Assuming the plane-wave mode within narrow channels, a general expression of sound transmission coefficient T can be derived as

$$T = \frac{2(\alpha_1\xi_1 + \alpha_2\xi_2)}{(1+\alpha_1\phi_1+\alpha_2\phi_2)^2 - (\alpha_1\xi_1+\alpha_2\xi_2)^2} \tag{1}$$

where $\xi_j = -i/\sin(kL_j)$, $\phi_j = -i\cot(kL_j)$, $\alpha_j = S_jZ_0/S_0Z_{ej}$, $S_0 = l_xl_y$, $S_j = a_jh$ with $j = 1, 2$. k and Z_{ej} denote, respectively, the wave vector and acoustic impedance [22], and they reduce to $k = \omega/c_0$, $Z_{ej} = Z_0 = \rho_0c_0$ in the absence of damping, where $\rho_0 = 1.21\,\mathrm{kg/m^3}$ and $c_0 = 343\,\mathrm{m/s}$ are, respectively, the density and sound velocity of air.

The channeling structure supports the resonant state, which can be disclosed by the transmission analysis for the waveguide system coupled to the single channel. In the dampless case, the acoustic transmission coefficient of the coiling channel is given by

$$T_c = \frac{2}{2\cos kL_2 + i(S_2/S_0 + S_0/S_2)\sin kL_2} \tag{2}$$

Equation (2) states that the coiling channel is in the resonant state when $\cos^2 kL_2 = 1$, which results in the resonant frequency

$$\omega_c^m = \frac{m\pi c_0}{L_2},\ m = 1, 2\ldots \tag{3}$$

where the integer m represents the order of resonant modes. At resonant frequencies ω_c^m, the transmission coefficient reads $T_c = (-1)^m$, which means that the resonant state is of monopole (dipole) mode when m is an odd (even) number. Similarly, the resonant frequency of the straight channel is given by

$$\omega_s^n = \frac{n\pi c_0}{L_1},\ n = 1, 2\ldots \tag{4}$$

Our study focuses on the coupling of resonant states supported by the coiling and straight channels. The coupled-mode theory will be adopted to establish an analytic model for the coupling system, by which a critical coupling condition for a low-transmission flat band will be disclosed.

2.2 Coupled-Mode Model. Consider the coupled-mode model where the mth-order resonant state of the coiling channel is coupled to the nth-order resonant state of the straight one. For brevity, denote the frequency and radiation loss of the resonant state supported by the coiling channel by ω_c and γ_c, respectively, and those of the straight channel by ω_s and γ_s. Modal amplitudes of two resonant states are denoted by a_c and a_s. Let s_L^+ and s_R^+ represent, respectively, wave amplitudes of sounds incident from the left and right sides, and s_L^- and s_R^- denote, respectively, those of outgoing waves scattered to the left and right, as schematically shown in Fig. 1(*b*). According to the temporal coupled-mode theory, the coupling system is governed by the dynamic equation

$$\begin{cases} -i\frac{d\mathbf{a}}{dt} = \mathbf{H}\mathbf{a} + \mathbf{K}^{\mathrm{T}}\mathbf{s}^+ \\ \mathbf{s}^- = \mathbf{C}\,\mathbf{s}^+ + \mathbf{D}\mathbf{a} \end{cases} \tag{5}$$

with

$$\mathbf{H} = \begin{bmatrix} \omega_c + i\gamma_c & im^+\sqrt{\gamma_c\gamma_s} \\ im^+\sqrt{\gamma_c\gamma_s} & \omega_s + i\gamma_s \end{bmatrix} \tag{6}$$

$$\mathbf{C} = \begin{bmatrix} 1 & 0 \\ 0 & 1 \end{bmatrix},\ \mathbf{K} = \begin{bmatrix} \sqrt{\gamma_c} & m_s\sqrt{\gamma_s} \\ m_c\sqrt{\gamma_c} & \sqrt{\gamma_s} \end{bmatrix},\ \mathbf{D} = i\mathbf{K} \tag{7}$$

where $\mathbf{a} = [a_c, a_s]^{\mathrm{T}}$, $\mathbf{s}^+ = [s_L^+, s_R^+]^{\mathrm{T}}$, $\mathbf{s}^- = [s_L^-, s_R^-]^{\mathrm{T}}$, and $m^+ = (m_c + m_s)/2$. $m_{c,s} = 1$ if the resonant state is of the monopole mode, and $m_{c,s} = -1$ for the dipole mode.

Based on Eq. (5), the acoustic scattering performance of the coupling system can be evaluated by the scattering matrix $\mathbf{S}$, which is given by

$$\mathbf{s}^- = \mathbf{S}\,\mathbf{s}^+,\quad \mathbf{S} = \mathbf{C} + \mathbf{D}(\omega\mathbf{I} - \mathbf{H})^{-1}\mathbf{K}^{\mathrm{T}} \tag{8}$$

According to Eq. (8), acoustic transmission coefficient $T = s_R^-/s_L^+$ is expressed as

$$T^{\mathrm{CM}} = \frac{im_c\gamma_c(\omega - \omega_s) + im_s\gamma_s(\omega - \omega_c)}{\det(\omega\mathbf{I} - \mathbf{H})} \tag{9}$$

where $\mathbf{I}$ is the identity matrix of rank two.

It can be derived from Eq. (9) that the zero transmission phenomenon ($T = 0$) appears at the degenerate frequency of two resonant states, namely $\omega = \omega_c = \omega_s$. Furthermore, the broadband zero transmission can be achieved when two resonant states are of different mode types and have the same radiation losses. The above broadband condition can be summarized as

$$\omega_c = \omega_s,\quad \gamma_c = \gamma_s,\quad m_c = -m_s \tag{10}$$

The critical coupling condition (10) is the key idea of the present study and will be explored to design the ventilation metamaterials with a low-transmission flat band.

2.3 Correlation Between Hamiltonian and Structural Parameters. To design acoustic metamaterials that fulfill the condition (10), it is necessary to establish the correlation between Hamiltonian parameters ($\omega_{c,s}$, $\gamma_{c,s}$) and geometric ones of channeling structures. This can be achieved by evaluating the coupled-mode model of single channels. Take the resonant state supported by the coiling channel as an example. Based on Eq. (5), acoustic transmission coefficient of the single-state system is given by

$$T_c^{\mathrm{CM}} = \frac{m_c\gamma_c}{i(\omega - \omega_c) + \gamma_c} \tag{11}$$

The correlation between ω_c, γ_c, and structural parameters can be established by comparing T_c of Eq. (2) with T_c^{CM}. For the coiling channel that operates in the mth-order resonant state, ω_c is equal to ω_c^m as expressed in Eq. (3), which is only relevant to the channel length L_2. $2\gamma_c$ measures the full width at half maximum

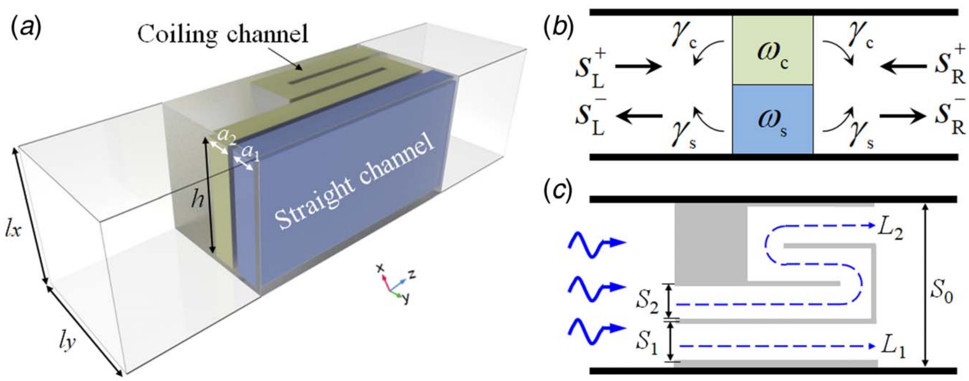

Fig. 1 (*a*) **Geometric model of acoustic metamaterial constructed by coupling the coiling and straight channels. (*b*) The coupled-mode model of the metamaterial. (*c*) Theoretical model for calculating acoustic transmission properties of the metamaterial.**

(FWHM) of the resonance peak centered at ω_c^m and satisfies the approximate relation $\gamma_c \approx \text{FWHM}/2$. The FWHM of the mth-order resonant state can be acquired by examining $|T_c|^2 = 1/2$, which results in

$$kL_2 = \frac{1}{2}\arccos(1 - 2B_2) \tag{12}$$

with

$$B_2 = \frac{4}{(S_2/S_0 + S_0/S_2)^2 - 4} \tag{13}$$

Equation (12) yields the frequency solutions

$$\omega_{\pm}^m = \pm\frac{c_0}{2L_2}\arccos(1 - 2B_2) + \omega_c^m \tag{14}$$

The radiation loss is given by $\gamma_c \approx (\omega_+^m - \omega_-^m)/2$, which results in

$$\gamma_c = \frac{c_0}{2L_2}\arccos(1 - 2B_2) \tag{15}$$

The Hamiltonian parameters ω_s and γ_s for the straight channel can be determined similarly. For the nth-order resonant state supported by the straight channel, ω_s is equal to ω_s^n as defined by Eq. (4), and γ_s is given by

$$\gamma_s = \frac{c_0}{2L_1}\arccos(1 - 2B_1) \tag{16}$$

where

$$B_1 = \frac{4}{(S_1/S_0 + S_0/S_1)^2 - 4} \tag{17}$$

According to the correlation relationships presented above, acoustic metamaterials with structural parameters that follow the critical coupling condition (10) can be designed as analyzed in the next section.

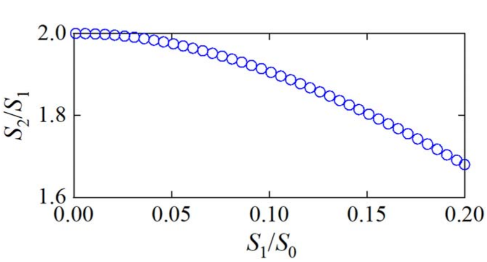

Fig. 2 Area ratio S_2/S_1 calculated by Eq. (18) for different values of S_1/S_0

3 Design of Metamaterials With Low-Transmission Flat Band

3.1 Metamaterials With the Lowest-Order Mode Coupling. Consider the coupling of monopole and dipole modes with the lowest-order $m = 2$ and $n = 1$. According to the critical coupling condition (10), the relation $L_2 = 2L_1$ can be derived from $\omega_c = \omega_s$, and the other condition $\gamma_c = \gamma_s$ leads to

$$1 - B_2 = (1 - 2B_1)^2 \tag{18}$$

Given the value S_1/S_0, the area ratio S_2/S_1 between two channels can be determined by Eq. (18) as plotted in Fig. 2. Now let us analyze the limit of $S_{1,2} \ll S_0$. It is observed that the area ratio converges to $S_2/S_1 = 2$, which is the same as the length ratio $L_2/L_1 = 2$. The coincidence motivates us to derive a general relation for the mth-order resonant state coupled to the nth-order one with different mode types. In the limit of $S_{1,2} \ll S_0$, there exists the following approximate relation:

$$\arccos(1 - 2B_i) \approx 4S_i/S_0 \tag{19}$$

Then, according to Eqs. (15) and (16), the critical coupling condition $\omega_c = \omega_s$ and $\gamma_c = \gamma_s$ is transformed to

$$L_2 : L_1 = S_2 : S_1 = m : n \tag{20}$$

Although Eq. (20) is derived in the limit of $S_{1,2} \ll S_0$, it is actually not limited to the small-area assumption in realistic structures as analyzed later by numerical examples. The primary reason is that the retrieval method for Hamiltonian parameters is based on a single channel without considering the potential influence of the other. Therefore, the condition given by Eq. (18) provides an approximate prediction, except in the limiting case of $S_{1,2} \ll S_0$, where the prediction is exact because the mutual influence between channels can be neglected.

As an example, the metamaterial with the lowest-order mode coupling ($m = 2$, $n = 1$) is designed to have geometric parameters $L_2 = 2L_1 = 34.3$ cm, $a_2 = 2a_1 = 17.14$ mm, $h = 7.2$ cm, and $l_x = l_y = 8$ cm. Figures 3(*a*) and 3(*b*) show, respectively, acoustic energy transmission of the waveguide system coupled to single and two channels as calculated by using Eq. (1) in the dampless case. It can be observed from Fig. 3(*a*) that the resonant frequencies of the first- and second-order modes are degenerate at 1 kHz, meanwhile the FWHM of two resonant peaks are equal, which means that the radiation losses of these two resonant states are same. Thus, the critical coupling condition (10) has been fulfilled. When such two channels are coupled, a low-transmission band centered at 1 kHz is formed as seen in Fig. 3(*b*). More strikingly, the band spectrum is flat with nearly zero sound transmission in accordance with the prediction by the coupled-mode model (9). Such a low-transmission behavior is completely different from the phenomena reported in

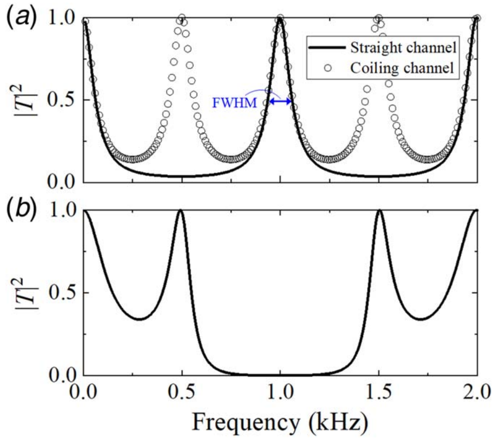

Fig. 3 Acoustic energy transmission of the waveguide system involving (*a*) single channel and (*b*) the coupled channels, which are calculated from Eq. (1) in the dampless case

previous models [32–40] and may be more preferable in noise control engineering.

3.2 Acoustic Transmission Analyses. Acoustic metamaterial presented in Fig. 3 has $S_1/S_0 \approx 0.1$, which has broken the small-area assumption, confirming the generality of the condition (20) for achieving the low-transmission flat band. Further demonstration is provided here through acoustic transmission analyses based on Eq. (1). In the absence of damping, the transmission coefficient T in Eq. (1) can be arranged as the factored form $T = T_\mathrm{A}T_\mathrm{B}$ with

$$T_\mathrm{A} = 2/(A_1 + iA_2), \quad T_\mathrm{B} = Y_1 - Y_2 \tag{21}$$

where

$$\begin{cases} Y_1 = S_{21}\sin X_1, \quad Y_2 = -\sin X_2, \quad S_{21} = S_2/S_1 \\ X_j = \omega L_j/c_0, \quad A_1 = 2(C_{21} + S_{21}C_{12}) \\ A_2 = \alpha_1\left[(1+S_{21}^2)C_{11} + 2S_{21}(1-C_{22})\right] + C_{11}/\alpha_1 \\ C_{11} = \sin X_1 \sin X_2, \quad C_{21} = \cos X_1 \sin X_2 \\ C_{12} = \sin X_1 \cos X_2, \quad C_{22} = \cos X_1 \cos X_2 \end{cases} \tag{22}$$

The term T_B is only relevant to the channel length $L_{1,2}$ and area $S_{1,2}$. Figure 4(*a*) plots the variation of Y_1 and Y_2 against frequency for the metamaterial designed in Fig. 3. There exists an overlapped frequency region between Y_1 and Y_2 that leads $|T_\mathrm{B}|$ approaching zero, while the magnitude of T_A remains finite as shown in Fig. 4(*b*). Thus, the low-transmission flat band can be formed as a result of the overlapping between Y_1 and Y_2. Figure 4(*b*) further shows the results of $|T_\mathrm{A}|$ when S_1/S_0 is changed to 0.06 and 0.08. The variation of S_1/S_0 would not alter the flat-band performance since the spectrum profile of Y_1 and Y_2 is preserved, but just affects the relative bandwidth, as illustrated in Fig. 4(*c*).

3.3 Simulation and Experimental Analyses. In previous examples, the low-transmission flat band is disclosed without considering acoustic damping. Below we carry out the analyses that take into account the viscous damping in narrow channels. Figure 5(*b*) shows the solid line acoustic transmission calculated from Eq. (1) for damped systems. Acoustic damping is found to induce only the decreasing of transmission peaks outside the valley region without the influence of the flat-band behavior. The flat-band acoustic isolation can be also verified by numerical simulations based on COMSOL Multiphysics, where the Narrow Region Acoustics module is adopted to simulate the viscous thermal losses within the channels. Simulation results are presented by the dashed line in Fig. 5(*b*) and are in good agreement with theoretical results.

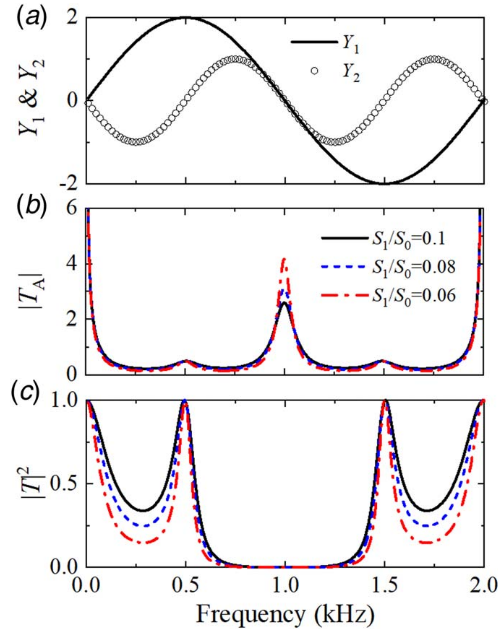

Fig. 4 (*a*) The spectrum profile of Y_1 and Y_2 against different frequencies. The frequency spectrum of (*b*) $|T_\mathrm{A}|$ and (*c*) $|T|^2$ in three different cases of S_1/S_0=0.06, 0.08, and 0.1.

In the experiment, the sample is fabricated by using 3D printing with Acrylonitrile Butadiene Styrene. Acoustic properties are measured by the impedance tube system as shown in Fig. 5(*a*). Experimental results of transmission coefficients of the sample are shown in Fig. 5(*b*) with circles, from which the flat band of low transmission can be clearly observed. According to Fig. 3(*a*), the monopole and dipole resonances degenerate at 1 kHz, leading to the cancellation effect for acoustic transmission. However, the interference cancellation between them is not perfect in the actual experiment as potentially influenced by the fabrication error and damping effect. Thereby, acoustic energy transmission near 1 kHz is a little bit higher than the average in the flat band. On the other hand, the upper band-edge frequency of the low-transmission band is higher than that predicted by theoretical and simulation results. Thus, the sound-isolation band broader than expected can be achieved in experiments. Let f_min and f_max denote, respectively, the lower and upper frequency of the band at which acoustic

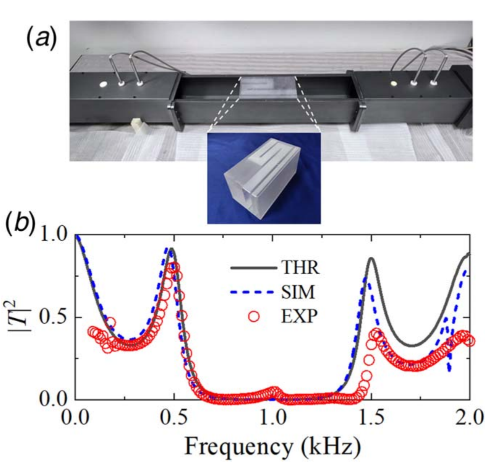

Fig. 5 (*a*) Experimental setup to measure acoustic transmission coefficients of the metamaterial sample. (*b*) Theoretical, simulation, and experimental results of acoustic transmission spectrum $|T|^2$.

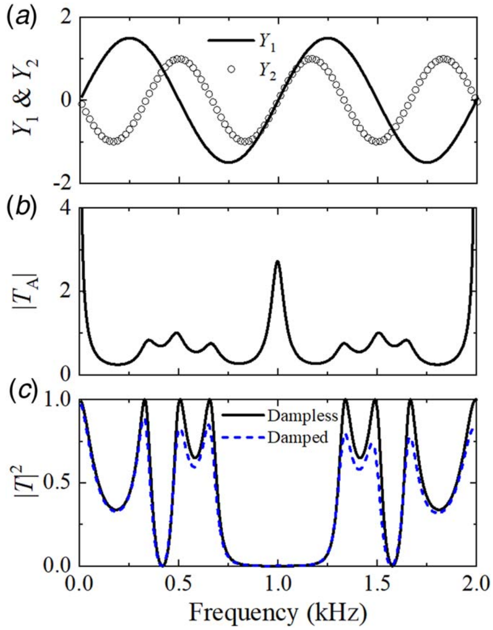

Fig. 6 The frequency spectrum of (*a*) $Y_{1,2}$ and (*b*) $|T_A|$ in the dampless case and (c) the transmission spectrum $|T|^2$ of the metamaterial with and without acoustic damping

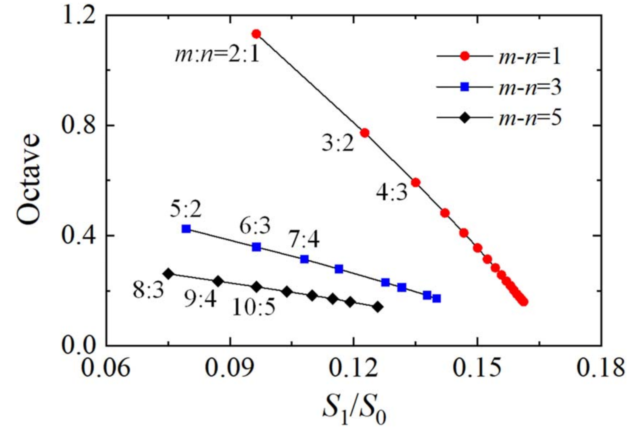

Fig. 7 Acoustic and ventilation properties of metamaterials with different mode couplings $m:n$, which are categorized into three groups with $m-n=1$, 3, 5, and generalized in the two-dimensional coordinates given by the octave bandwidth and S_1/S_0

energy transmission is lower than 0.1. The bandwidth in octaves can be defined as $\mathrm{Log}_2(f_{\max}/f_{\min})$. According to Fig. 5(*b*), the experimental octave bandwidth is up to 1.278, and the thickness of the sample is about 1/1.94 of the wavelength of the band center frequency.

3.4 Metamaterials With High-Order Mode Couplings. We proceed to analyze the metamaterial with high-order mode couplings by considering $m=3$ and $n=2$. Geometric parameters of the designed metamaterial are $L_2=1.5L_1=51.45$ cm, $a_2=1.5a_1=16.35$ mm, $h=7.2$ cm, and $l_x=l_y=8$ cm. Figures 6(*a*) and 6(*b*) show, respectively, the frequency spectrum of $Y_{1,2}$ and $|T_A|$ in the dampless case. The curves for Y_1 and Y_2 overlap in a finite region near the degenerate frequency 1 kHz of two modes, meanwhile the amplitude of T_A remains finite. Therefore, the low-transmission flat band can be also realized as demonstrated in Fig. 6(*c*), which displays the transmission spectrum $|T|^2$ with and without acoustic damping. The intrinsic damping is seen to affect only the resonant transmission outside the flat sound-isolation band.

The air ventilation rate is closely related to the area ratio between the straight channel and waveguide S_1/S_0. Thus, acoustic and ventilation properties of metamaterials with different mode couplings $m:n$ can be generalized in the two-dimensional coordinates given by the octave bandwidth and S_1/S_0. Based on numerical simulations with acoustic damping, metamaterials with mode couplings $2:1$ and $3:2$ as analyzed in Figs. 5 and 6 are plotted in Fig. 7. Notice that S_1/S_0 is not unique given the area ratio $S_2:S_1=m:n$. In examples given previously, the largest ventilation ratio (S_1/S_0) has been selected among all geometries where the coiling channel is of the reverse-Z-shaped pattern, as sketched in Fig. 1(*a*). Following the above protocol, metamaterials with various mode couplings are categorized into three groups with $m-n=1$, 3, 5, and the results are summarized in Fig. 7. The group with $m-n=1$ is superior than others as it has a wider isolation bandwidth and larger ventilation rate. The octave bandwidth and S_1/S_0 for each group are inversely proportional. Metamaterials with high-order mode couplings tends to achieve better air ventilation performance yet with the decreasing of the isolation bandwidth.

3.5 Metamaterials With Side-Branch Structures. The critical coupling condition (20) for achieving the low-transmission flat band is only relevant to the mode coupling between the coiling and straight channels. In principle, it should not be just

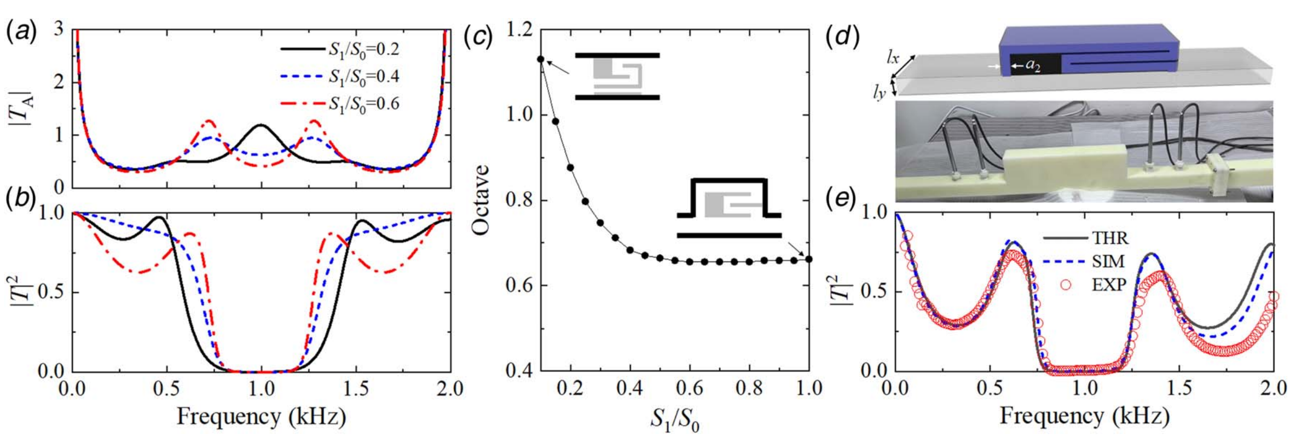

Fig. 8 (*a*) The frequency spectrum of $|T_A|$ in cases of S_1/S_0=0.2, 0.4, and 0.6. (*b*) The corresponding transmission spectrum $|T|^2$ of the metamaterial with acoustic damping. (*c*) Octave bandwidth of the metamaterial with side enlargements calculated for various S_1/S_0. (*d*) Experimental setup for measuring acoustic transmission properties of the metamaterial with the side-branch structure. (*e*) Theoretical, simulation, and experimental results of acoustic energy transmission $|T|^2$ of the side-loaded metamaterial.

limited to the configuration that the coiling channel is embedded within the waveguide. Take the metamaterial with the lowest mode coupling ($m = 2$, $n = 1$) as an example. This viewpoint can be proven true in Fig. 8(*a*), which shows the results of $|T_A|$ for different values of S_1/S_0= 0.2, 0.4, and 0.6. Here, the values of S_1/S_0 are all beyond the threshold 0.1 such that the coiling channel will occupy partially the external region of the waveguide. $|T_A|$ remains finite in each case, and the spectrum behavior of Y_1 and Y_2 that leads to the flat band still follows Fig. 4(*a*) irrelevant to the area ratio S_1/S_0. Thereby, acoustic transmission $|T|^2$ exhibits again the low-transmission flat-band phenomenon as presented in Fig. 8(*b*). Acoustic isolation properties of metamaterials with side enlargements can also be characterized by the octave bandwidth. Figure 8(*c*) shows the bandwidth results for various S_1/S_0 based on numerical simulations with acoustic damping. With the increase in S_1/S_0, the sound-isolation bandwidth drops to a stable value 0.66; yet, more significantly, the air ventilation rate can be greatly enhanced.

In the limiting case of S_1/S_0= 1, the coiling channel will be placed completely in the external region of the waveguide, as sketched in the inset of Fig. 8(*c*). The straight waveguide with the side-branch structure then constitutes an important sound silencing model widely used for acoustic liners to damp engine noise. Experimental studies are carried out for this metamaterial as shown in Fig. 8(*d*). Geometric parameters of the system are chosen as $l_x = 12$ mm, $l_y = 6$ mm, $L_2 = 2L_1 = 68.6$ cm, and $a_2 = 12$ mm. The sample and waveguide system are fabricated by using 3D printing. Figure 8(*e*) shows the theoretical, simulation, and experimental results of acoustic energy transmission $|T|^2$ of the side-loaded metamaterial with the mode coupling of $m = 2$ and $n = 1$. The measurement results confirm the low-transmission flat band with the octave bandwidth of 0.645 and are in good agreement with theoretical and simulation predictions. This flat-band metamaterial allows the perfect air flow within the waveguide and provides a new mechanism for the design of broadband low-frequency duct silencers.

4 Conclusions

Acoustic metamaterials consisting of the coiling and straight channels are studied for simultaneous control of sound mitigation and air ventilation. When two channels both work in acoustic resonant states, a critical coupling condition that can lead to the flat-band behavior of the near-zero transmission is found based on the coupled-mode theory. Experimental results demonstrate the flat-band effect in metamaterials with the lowest-order mode coupling, realizing the octave bandwidth up to 1.278. The generality of the flat-band behavior is then verified in metamaterials with high-order mode couplings, where there is a trade-off between sound-isolation bandwidth and air ventilation rate. Finally, we extend the metamaterial model in the way by placing the coiling channel completely in the external region of the waveguide and validate the flat-band behavior experimentally. The proposed mechanism paves the way toward the novel design of broadband low-frequency sound-isolation devices.

Acknowledgment

This work was supported by the National Natural Science Foundation of China (12225203, 11622215, 11872111, 11991030, and 11991033) and 111 Project (B16003).

Conflict of Interest

There are no conflicts of interest.

Data Availability Statement

The datasets generated and supporting the findings of this article are obtainable from the corresponding author upon reasonable request.

References

[1] Ghaffarivardavagh, R., Nikolajczyk, J., Glynn Holt, R., Anderson, S., and Zhang, X., 2018, "Horn-Like Space-Coiling Metamaterials Toward Simultaneous Phase and Amplitude Modulation," Nat. Commun., **9**(1), p. 1349.
[2] Xie, Y., Wang, W., Chen, H., Konneker, A., Popa, B.-I., and Cummer, S. A., 2014, "Wavefront Modulation and Subwavelength Diffractive Acoustics With an Acoustic Metasurface," Nat. Commun., **5**(1), p. 5553.
[3] Li, Y., Jiang, X., Li, R.-Q., Liang, B., Zou, X.-Y., Yin, L.-L., and Cheng, J.-C., 2014, "Experimental Realization of Full Control of Reflected Waves With Subwavelength Acoustic Metasurfaces," Phys. Rev. Appl., **2**(6), p. 064002.
[4] Lu, D., and Liu, Z., 2012, "Hyperlenses and Metalenses for Far-Field Super-Resolution Imaging," Nat. Commun., **3**(1), p. 1205.
[5] Zhu, J., Christensen, J., Jung, J., Martin-Moreno, L., Yin, X., Fok, L., Zhang, X., and Garcia-Vidal, F., 2011, "A Holey-Structured Metamaterial for Acoustic Deep-Subwavelength Imaging," Nat. Phys., **7**(1), pp. 52–55.
[6] Cummer, S. A., Popa, B. -I., Schurig, D., Smith, D. R., Pendry, J., Rahm, F. M., and Starr, A., 2008, "Scattering Theory Derivation of a 3D Acoustic Cloaking Shell," Phys. Rev. Lett., **100**(2), p. 024301.
[7] Chen, H., and Chan, C. T., 2007, "Acoustic Cloaking in Three Dimensions Using Acoustic Metamaterials," Appl. Phys. Lett., **91**(18), p. 183518.
[8] Dong, J., Zhao, Y., Cheng, Y., and Zhou, X., 2018, "Underwater Acoustic Manipulation Using Solid Metamaterials With Broadband Anisotropic Density," ASME J. Appl. Mech., **85**(12), p. 121007.
[9] Yang, M., and Sheng, P., 2017, "Sound Absorption Structures: From Porous Media to Acoustic Metamaterials," Annu. Rev. Mater. Res., **47**(1), pp. 83–114.
[10] Liu, C., Shi, J., Zhao, W., Zhou, X., Ma, C., Peng, R., Wang, M., Hang, Z. H., Liu, X., Christensen, J., Fang, N. X., and Lai, Y., 2021, "Three-Dimensional Soundproof Acoustic Metacage," Phys. Rev. Lett., **127**(8), p. 084301.
[11] Xu, Z.-X., Gao, H., Ding, Y.-J., Yang, J., Liang, B., and Cheng, J.-C., 2020, "Topology-Optimized Omnidirectional Broadband Acoustic Ventilation Barrier," Phys. Rev. Appl., **14**(5), p. 054016.
[12] Ma, G., Yang, M., Yang, Z., and Sheng, P., 2013, "Low-Frequency Narrow-Band Acoustic Filter With Large Orifice," Appl. Phys. Lett., **103**(1), p. 011903.
[13] Cheng, Y., Zhou, C., Yuan, B., Wu, D., Wei, Q., and Liu, X., 2015, "Ultra-Sparse Metasurface for High Reflection of Low-Frequency Sound Based on Artificial Mie Resonances," Nat. Mater., **14**(10), pp. 1013–1019.
[14] Yang, M., Meng, C., Fu, C., Li, Y., Yang, Z., and Sheng, P., 2015, "Subwavelength Total Acoustic Absorption With Degenerate Resonators," Appl. Phys. Lett., **107**(10), p. 104104.
[15] Wang, X., Luo, X., Yang, B., and Huang, Z., 2019, "Ultrathin and Durable Open Metamaterials for Simultaneous Ventilation and Sound Reduction," Appl. Phys. Lett., **115**(17), p. 171902.
[16] Lee, T., Nomura, T., Dede, E. M., and Iizuka, H., 2019, "Ultrasparse Acoustic Absorbers Enabling Fluid Flow and Visible-Light Controls," Phys. Rev. Appl., **11**(2), p. 024022.
[17] Wu, X., Au-Yeung, K. Y., Li, X., Roberts, R. C., Tian, J., Hu, C., Huang, Y., Wang, S., Yang, Z., and Wen, W., 2018, "High-Efficiency Ventilated Metamaterial Absorber at Low Frequency," Appl. Phys. Lett., **112**(10), p. 103505.
[18] Shen, C., Xie, Y., Li, J., Cummer, S. A., and Jing, Y., 2018, "Acoustic Metacages for Sound Shielding With Steady Air Flow," J. Appl. Phys., **123**(12), p. 124501.
[19] Xiang, X., Tian, H., Huang, Y., Wu, X., and Wen, W., 2021, "Manually Tunable Ventilated Metamaterial Absorbers," Appl. Phys. Lett., **118**(5), p. 053504.
[20] Ma, G., Yang, M., Xiao, S., Yang, Z., and Sheng, P., 2014, "Acoustic Metasurface With Hybrid Resonances," Nat. Mater., **13**(9), pp. 873–878.
[21] Merkel, A., Theocharis, G., Richoux, O., Romero-García, V., and Pagneux, V., 2015, "Control of Acoustic Absorption in One-Dimensional Scattering by Resonant Scatterers," Appl. Phys. Lett., **107**(24), p. 244102.
[22] Zhang, R., Wang, G., Zhou, X., and Hu, G., 2022, "A Decoupling-Design Strategy for High Sound Absorption in Subwavelength Structures With Air Ventilation," JASA Express Lett., **2**(3), p. 033602.
[23] Nguyen, H., Wu, Q., Xu, X., Chen, H., Tracy, S., and Huang, G., 2020, "Broadband Acoustic Silencer With Ventilation Based on Slit-Type Helmholtz Resonators," Appl. Phys. Lett., **117**(13), p. 134103.
[24] Dong, R., Mao, D., Wang, X., and Li, Y., 2021, "Ultrabroadband Acoustic Ventilation Barriers via Hybrid-Functional Metasurfaces," Phys. Rev. Appl., **15**(2), p. 024044.
[25] Li, L.-J., Zheng, B., Zhong, L.-M., Yang, J., Liang, B., and Cheng, J.-C., 2018, "Broadband Compact Acoustic Absorber With High-Efficiency Ventilation Performance," Appl. Phys. Lett., **113**(10), p. 103501.
[26] Kim, D.-Y., and Ih, J.-G., 2020, "Wideband Reduction of In-Duct Noise Using Acoustic Metamaterial With Serially Connected Resonators Made With MPP and Cavities," Appl. Phys. Lett., **116**(25), p. 251904.
[27] Xiang, X., Wu, X., Li, X., Wu, P., He, H., Mu, Q., Wang, S., Huang, Y., and Wen, W., 2020, "Ultra-Open Ventilated Metamaterial Absorbers for Sound-Silencing Applications in Environment With Free Air Flows," Extreme Mech. Lett., **39**, p. 100786.
[28] Lee, T., Nomura, T., Dede, E. M., and Iizuka, H., 2020, "Asymmetric Loss-Induced Perfect Sound Absorption in Duct Silencers," Appl. Phys. Lett., **116**(21), p. 214101.
[29] Kumar, S., and Lee, H. P., 2020, "Labyrinthine Acoustic Metastructures Enabling Broadband Sound Absorption and Ventilation," Appl. Phys. Lett., **116**(13), p. 134103.

[30] Dong, R., Sun, M., Mo, F., Mao, D., Wang, X., and Li, Y., 2021, "Recent Advances in Acoustic Ventilation Barriers," J. Phys. D: Appl. Phys., **54**(40), p. 403002.
[31] Jiménez, N., Romero-García, V., Pagneux, V., and Groby, J.-P., 2017, "Rainbow-Trapping Absorbers: Broadband, Perfect and Asymmetric Sound Absorption by Subwavelength Panels for Transmission Problems," Sci. Rep., **7**(1), p. 13595.
[32] Chen, A., Zhao, X., Yang, Z., Anderson, S., and Zhang, X., 2022, "Broadband Labyrinthine Acoustic Insulator," Phys. Rev. Appl., **18**(6), p. 064057.
[33] Ghaffarivardavagh, R., Nikolajczyk, J., Anderson, S., and Zhang, X., 2019, "Ultra-Open Acoustic Metamaterial Silencer Based on Fano-Like Interference," Phys. Rev. B, **99**(2), p. 024302.
[34] Sun, M., Fang, X., Mao, D., Wang, X., and Li, Y., 2020, "Broadband Acoustic Ventilation Barriers," Phys. Rev. Appl., **13**(4), p. 044028.
[35] Zhang, H.-L., Zhu, Y.-F., Liang, B., Yang, J., Yang, J., and Cheng, J.-C., 2017, "Omnidirectional Ventilated Acoustic Barrier," Appl. Phys. Lett., **111**(20), p. 203502.
[36] Dong, R., Mao, D., Zhu, Y., Mo, F., Wang, X., and Li, Y., 2021, "A Ventilating Acoustic Barrier for Attenuating Broadband Diffuse Sound," Appl. Phys. Lett., **119**(26), p. 263505.
[37] Xu, Z.-X., Zheng, B., Yang, J., Liang, B., and Cheng, J.-C., 2021, "Machine-Learning-Assisted Acoustic Consecutive Fano Resonances: Application to a Tunable Broadband Low-Frequency Metasilencer," Phys. Rev. Appl., **16**(4), p. 044020.
[38] Nguyen, H., Wu, Q., Chen, H., Chen, J., Yu, Y., Tracy, S., and Huang, G., 2021, "A Fano-Based Acoustic Metamaterial for Ultra-Broadband Sound Barriers," Proc. R. Soc. A, **477**(2248), p. 20210024.
[39] Tang, Y., Liang, B., and Lin, S., 2022, "Broadband Ventilated Meta-Barrier Based on the Synergy of Mode Superposition and Consecutive Fano Resonances," J. Acoust. Soc. Am., **152**(4), pp. 2412–2418.
[40] Xu, Z.-X., Qiu, W.-J., Cheng, Z.-Q., Yang, J., Liang, B., and Cheng, J.-C., 2024, "Broadband Ventilated Sound Insulation Based on Acoustic Consecutive Multiple Fano Resonances," Phys. Rev. Appl., **21**(4), pp. 044049.